UNIVERSITY OF CALIFORNIA

SANTA CRUZ

NON-INVASIVE SINGLE-CELL ACOUSTO-MECHANOPHENOTYPING

A thesis submitted in partial satisfaction of the

requirement for the degree of

MASTER OF SCIENCE

in

ELECTRICAL & COMPUTER ENGINEERING

by

Le Luo

June 2020

The Thesis of Le Luo

is approved:

_____

Professor Ahmet Ali Yanik, Chair

_____

Professor Michael Wehner

_____

Professor Shiva Abbaszadeh

_____

Quentin Williams

Acting Vice Provost and Dean of Graduate Studies

Table of Contents

List of Figures

Abstract

Non-Invasive Single-Cell Acousto-Mechanophenotyping

by

Le Luo

Living cells undergoing cellular differentiation, chronological aging, and malignant progression could exhibit dramatically different biophysical characteristics. Accurate quantification of the intrinsic mechanical properties of cells is of both practical and fundamental significance in biological research and clinical diagnostics. Here, we introduce Non-invaSIve acousTo-mechanophEnotyping (ON-SITE) for high-throughput (~ 5×10^4 cells/hr) on-the-fly quantification of single-cell mechanics in continuous flow without any physical contact and labeling. ON-SITE integrates two sequential modes of acousto-dynamic operation in a staged fashion, enabling three-dimensional focusing of cells into a tight line and subsequent touchless steering of them orthogonal to laminar flow, tracing out a parabola-like trajectory. This unique dual functionality offers real-time probing and evaluation of cell mechanical properties with excellent spatiotemporal resolution by tracking cell axial transit path lengths over its entire trajectory. We identified multiple critical biophysical factors (size, density, compressibility) that contribute to the dynamic motion of cells by analytical modeling and experimental approaches. We demonstrate highly efficient, reliable,

and precise quantification of the cell elastic modulus of three distinct wild-type hematopoietic progenitors and their conditionally reprogrammed counterparts upon treatment with cytoskeleton-perturbing molecules. Remarkably, the subtle microscopic differences (~ 1 – 12 %) in cell elastic modulus are unraveled on an ultrafast timescale (~ 0.3 s) using acoustic waves that are generated at a clinically safe power (~ 2 W/cm^2) and frequency (~ 13 MHz) level.

Acknowledgements

I would like to express my deepest gratitude to my M.S. advisor, Professor Ahmet Ali Yanik for his constant supervision, support, tolerance and trust. I would also like to thank him for providing me with the opportunities to explore some exciting research fields in his group. I learnt a lot from his wisdom and experience, which will be of great help in my future academic career. Lastly, I would like to thank his supervision, support, trust, and tolerance.

I would like to thank Professors Michael Wehner and Shiva Abbaszadeh, in the Department of Electrical and Computer Engineering, for their constructive feedback on my thesis work. I would also like to thank them for their kindness and academic guidance during my time at the University.

To my colleague, Dr. Xiangchao "Jude" Zhu, for primarily guiding me with my research, and for his friendship. Your supervision, guidance, and passion has truly inspired me to strive for excellence in scientific research. Thank you very much for your help.

To my colleague, Yixiang "Louis" Li, for teaching me important skills in the lab and taking the time to guide me step by step. Your contribution played an important role in the whole project. Without your help, I may not learn these precious skills in research, to complete my masters. I will always remember your advice and suggestion when I face obstacles in my future.

I would also like to thank you my friends, and colleagues in the UCSC Nanoengineering group. My friend and colleague, Ray Jara, always encouraged me when I was in dilemma or felt pessimistic about a project. My friend, Jose Fuentes gave me the assistance and knowledge on how to optimize my device for the best performance. My friend, Mustafa Mutlu offered a great deal assistance for the arrangement of thesis defense. I would also like to thank the rest of the community in Santa Cruz for accepting me into the community and letting me experience its environment.

Finally, I would like to acknowledge the supports and sacrifices from my family so that I can pursue my academic career away from home. Their understanding, supports and love gave the me strength to overcome various problems and push forward. Now that, I am going to graduate with a master degree in ECE, I want to thank my family here.

Chapter 1

Introduction and Background

1.1 Motivation

Cell mechanics plays a vital role in the coordination of many cellular behaviors during a diverse array of biological processes, including pathological progression, tissue remodeling, and morphogenesis[1-3]. Measurement of cell mechanics offers fundamental and key insights into the reciprocity of mechanical and biological interactions at various hierarchical levels[4-6]. Furthermore, it constitutes an attractive non-invasive biomarker for identification of cell populations, eliminating the need for extrinsic labels[7]. Recent findings suggest that alterations of cell mechanical properties in response to applied mechanical stresses (e.g. heart pumping, fluid shear stress)[8, 9] are hallmarks of various dynamic cell functions (e.g. leukocyte activation, migration and cell differentiation)[7, 10] and pathophysiological phenotypic transformations (e.g. cancer and cardiovascular disease)[11, 12]. In this respect, development of tools for mapping heterogeneity of cellular mechanics rapidly and accurately has immense potential to reveal new targets for regenerative therapies, cancer diagnostics, pulmonary and cardiovascular disease, and stem cell biology. Modern mechanophenotyping technologies include gold standard atomic force microscopy[12, 13] and micropipette aspiration[14, 15], as well as microfluidics-based optical stretching[16-18], particle-

tracking microrheology[19-22], deformability cytometry[23]. These methods enable extraction of cellular mechanical properties (elastic modulus, viscosity) from whole cell to local length-scales by evaluating time-resolved cell responses to a calibrated force or physical deformation[9, 12, 24]. Yet, quantitative assessment of multiple mechanical properties from a large population of living cells with similar spatiotemporal resolution in a non-invasive, high-throughput manner remains challenging. These existing mechanophenotyping techniques either suffer from low measurement throughput (a few to tens of cells per hour) due to technically demanding and time-consuming procedures, or could cause trauma/damage to cells as direct contact with the cells of interest is required. Furthermore, they do not provide well-controlled mechanical loading conditions and non-specific interactions between the probe and the cell surface, rendering measurement statistically unreliable.

1.2 Mechanical properties of single cells

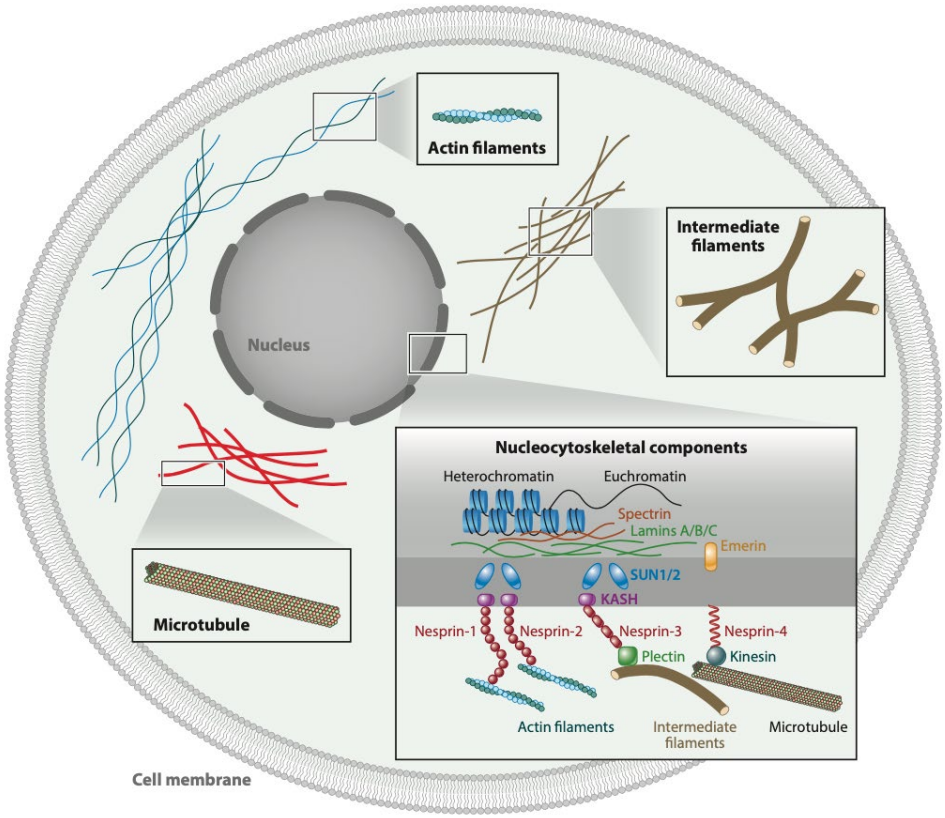

Figure 1.2.1: The schematic of internal components of individual cells determines the cellular mechanical phenotypes. Cellular mechanical and biological characteristics depend on the major cytoskeletal elements, including microfilaments, microtubules and intermediate filaments. Adapted from the article[25].

The mechanical behavior of individual cells plays an extremely important role in historically being given to the cytoskeleton. It is closely linked to intracellular components, determining the phenomena of mechanosensing and mechanotransduction. Understanding the mechanical properties relied on the

connections among membrane proteins, the cytoskeleton, and the nucleus can demonstrate the mechanical behavior of cells[25]. Cytoskeleton mainly consists of microfilaments, microtubules and intermediate filaments, protecting deformation of individual cells by the external stimuli. Cell membrane has tremendous connections with various organs so that it is vital contributor to cellular mechanical behavior. Nucleus, a primary part of cells, influences mechanical property measurements. Therefore, understanding mechanical properties among these components of cells is very important to explore the mechanism of protection, differentiation of cells and mechanical behavior of living cells.

1.3 Modern Mechanophenotyping Techniques

The recent decade has witnessed the fantastic development of mechanophenotyping technologies, such as atomic force microscopy (AFM), micropipette aspiration (MA), and optical tweezers (OTs), enabling biomarker-free decoding of mechanical fingerprints of single cells. As for AFM and MA, they can be used to measure the Young's modulus of a cell. But AFM requires contacting cells directly by a cantilever tip so that it tests cells adhered in a surface and MA requires testing cells in suspension via suction. OTs facilitates measurement of mechanical properties with high-throughput by associating with microfluidic system and it also can be used in sorting or separating cells among microchannels[25].

1.3.1 Atomic Force Microscopy (AFM)

AFM, shown in figure 1.3.1, is a mechanical method invented by Gerd Binning in 1986 for high-resolution imaging of surface of living and fixing cells[26].

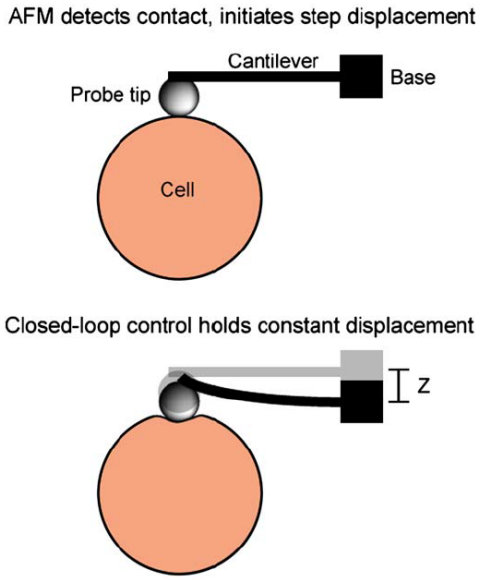

Figure 1.3.1: Illustration of AFM. Measuring the deflection z of the cantilever tip to calculate indentation force and get mechanical properties subsequently. Adapted from the article[26].

Its unique point is that it has proven to be an instrument which can be applied with image biological systems at high resolution[27]. The deformation of a cell is determined by physical indentation or compression. The indentation force relies on the deflection of the cantilever tip, which is measured optically and calculated via Hooke's law ($F = kx$). Even though AFM precisely measures physical properties of portion of individual cells in a highly controlled surrounding, it requires the tip to touch a cell and then deform it, including direct contact with the cell. Target cell will be damaged and the measurements could be affected by the contact because

AFM produces stiff force compare to the stiffness of the cell surface. Besides, the high-resolution imaging requires expensive devices with professional function.

1.3.2 Micropipette Aspiration (MA)

A common indentation-type mechanical measurement of single cells is micropipette aspiration, known as MA. MA involves applying suction pressure to a cell and monitoring the extension of the membrane into the bore of a micropipette[15]. As opposed to AFM, MA can be used to high throughput applications since its compatibility with microfluidic designs expands its original field of applications[28]. MA is able to create a deformation which is the opposite of that produced by AFM in the cell surface. The deformation, being extended into the pipette rather than the interior of the cell is sucked by a biointerface probe[15]. The principle of MA is shown in Figure 1.3.2:

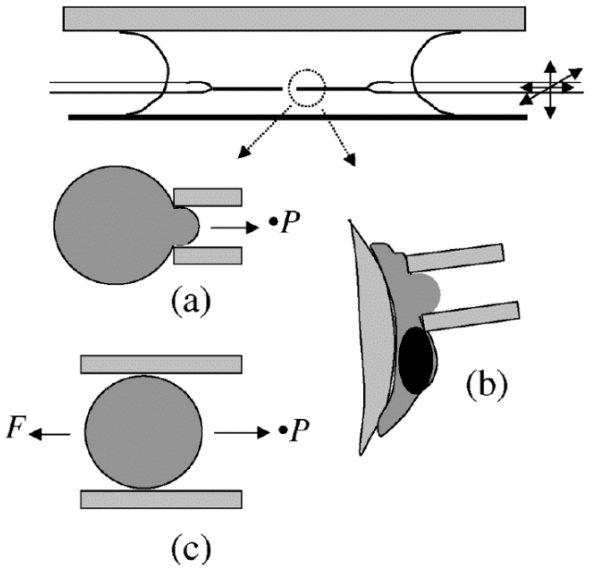

Figure 1.3.2: Putting two micropipettes in a chamber. The movement of a micropipette is controlled by a pneumatic micromanipulator. (a) shows that a spherical cell is aspirated into a micropipette. The suction pressure is ΔP. (b) demonstrates that an irregular cell is aspirated into a micropipette. (c) explains a cell moving freely in a pipette after aspiration. The force F can be measured by suction pressure and the crossed area in a static situation. Adapted from the article[15].

However, MA is limited to creep experiments because of its property of natural design. It is less versatile in the diversities of targets so it is confined in specific realms[25]. Micropipettes contacting cells may affect cytoactive and its any local deformation will influence the measurement, resulting in low throughput and unprecise experimental data.

1.3.3 Optical tweezers (OTs)

Light-based approaches, optical tweezers (OTs) is very different from AFM and MA because it does not have to require mechanical contact with samples[25, 29]. Utilizing a highly focused laser beam is utilized to create a 3D light gradients, exert attractive and repulsive force on a sample. Conventional OTs is limited by the size of particles because of the manipulation using a single trip, but OTs is also optimized by integrated into microfluidic systems, which makes a breakthrough at the conventional point[30]. Figure 1.3.3 shows the principle of OTs:

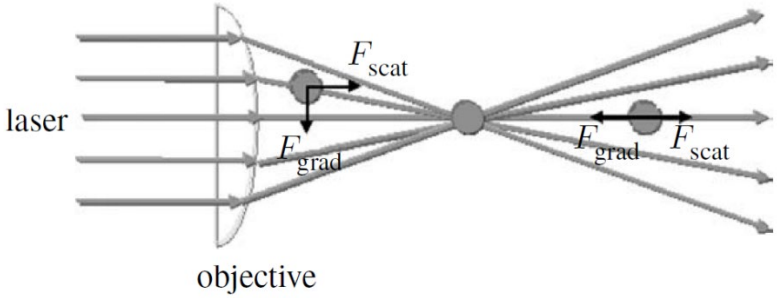

Figure 1.3.3: Schematic of OTs. Light is focused to diffraction-limited beam waist after entering the objective lens of a microscope, and it creates a three-dimensional gradient. A particle escapes out of trap and then it is brought back to the center of trap. Adapted from the article[29].

The scattering force produced by the photons strikes the cell along their propagation direction while the gradient force produced by a gradient of field intensity drags the cell[29]. OTs are relatively easy to measure the mechanical properties of cells in suspension. However, the approaches' shortcomings are

obvious that OTs requires complex optical devices and instruments as well as sophisticated image processing systems require expensive instruments. As for the throughput, the limitation of using OTs to measure physical properties of cells is the magnitude of the applied force, implementing less than a couple of hundred piconewtons. The force is not strong enough to deform most cell types so that experimental results may lost some important information for the whole-cell properties[25]. There is a table shown below discussing the summary of these conventional techniques for mechanical properties of individual cells, which is given in Table 1:

Technique	Deformation	Unique Feature	Drawback
Atomic Force Microscope (AFM)	Interior (< 2.5% of a single cell)	Highly localized measurement (<2% of cell); precise measurement in highly controlled environment	low-throughput (~10 cells/hr); Invasive; Alternative tests for describing the target cell's deformation behavior
Micropipette Aspiration (MA)	External (~50% of a single cell)	Conductive with high-throughput due to its compatibility with microfluidic design	low-throughput (~10 cells/hr); Invasive; Less versatile for the various types of cells
Optical Tweezers (OTs)	Interior (< 0.5 μm^3)	Measurement with high resolution (~5 μm); Integrated into microfluidic system	low-throughput (~10 cells/hr); Photodamage (invasive); Limitation by applied small-magnitude force

Table 1: Summary of modern mechanophenotyping techniques to measure mechanical properties of single cells.

1.4 Non-Invasive Acousto-Mechanophenotyping

Here, we introduce nON-invaSIve acousTo-mechanophEnotyping (ON-SITE) for in-situ, label-free, on-flight, robust, accurate, and high-throughput (~ 5×10^4 cells/hr) quantification of cellular mechanical properties. Our ON-SITE platform, offering non-contact and non-destructive handling of living cells with excellent spatiotemporal resolution, enables quantitative analysis of single-cell mechanics over multiple differentiated cell types and their conditionally reprogrammed counterparts with subcellular modulation of intracellular cytoskeleton contractility. Unlike the recently proposed acoustic methods[31-34], our ON-SITE technique provides direct quantitative measurement of the elastic modulus of living cells (that is compressibility). Furthermore, our acoustic assay is ideally suited for identification and discrimination of heterogeneous populations owing to its capacity to decouple various biophysical factors (cell size, density) from modulus effect, significantly reducing measurement variability. In contrast to the existing acoustic platforms that require materials with excellent acoustic reflection properties, our acoustic platform permits rapid designing and prototyping and is easy to assemble and use with great convenience. Using a regular inverted microscope setup equipped with a monochrome digital camera, we capture the full dynamics of suspended cells with heterogeneous size/density/compressibility on-the-fly. By employing a two-level cascade acousto-dynamic configuration, we achieve three-dimensional (3D) tight focusing of cells that pass two distinct 3D

standing acoustic fields consecutively in a microfluidic channel. We show that cell compressibility can be rapidly and accurately determined by evaluating the axial transit path length over which an individual cell migrates with constant speed between two predesignated equilibrium positions, where lateral movement transverse to laminar flow ceases. In this work, we study the mechanical properties of bone marrow derived hematopoietic stem cells (HSCs), myeloid progenitors (MyPros), and macrophages (Macs) due to their important significance for clinical purposes such as treatment of multiple myeloma and autoimmune disorders[35-38]. We exploit ON-SITE to identify and distinguish HSCs from differentiated MyPros and mature Macs. We discover the correlation between cellular mechanical properties and the hierarchical level of hematopoietic cells: cell compressibility becomes higher and cell-cell variability in compressibility within a single cell type diminishes with decreasing level of hematopoietic hierarchy. In addition, we investigate the mechanical properties of these hematopoietic cell types that are reprogrammed by Rho-kinase (ROCK) inhibition treatment that reorganizes cellular actin cytoskeleton. We show that the reprogrammed cells exhibit a higher compressibility and considerably lower level of cell-cell variability in compressibility. Using a Modified Boyden Transwell chamber assay, we demonstrate that ROCK inhibition treatment serves as an effective way to improve cell migratory ability, which is an important cellular function that is essential to a variety of biological processes (e.g. organogenesis). ON-SITE represents an easy

to implement, direct, and efficient means to quantify various cellular mechanical properties from heterogeneous populations, providing an effective avenue for future fundamental studies in cell mechanobiology and in the functional impact of drug treatment on cell signaling and phenotype. The illustration is shown in Figure 1.4.1:

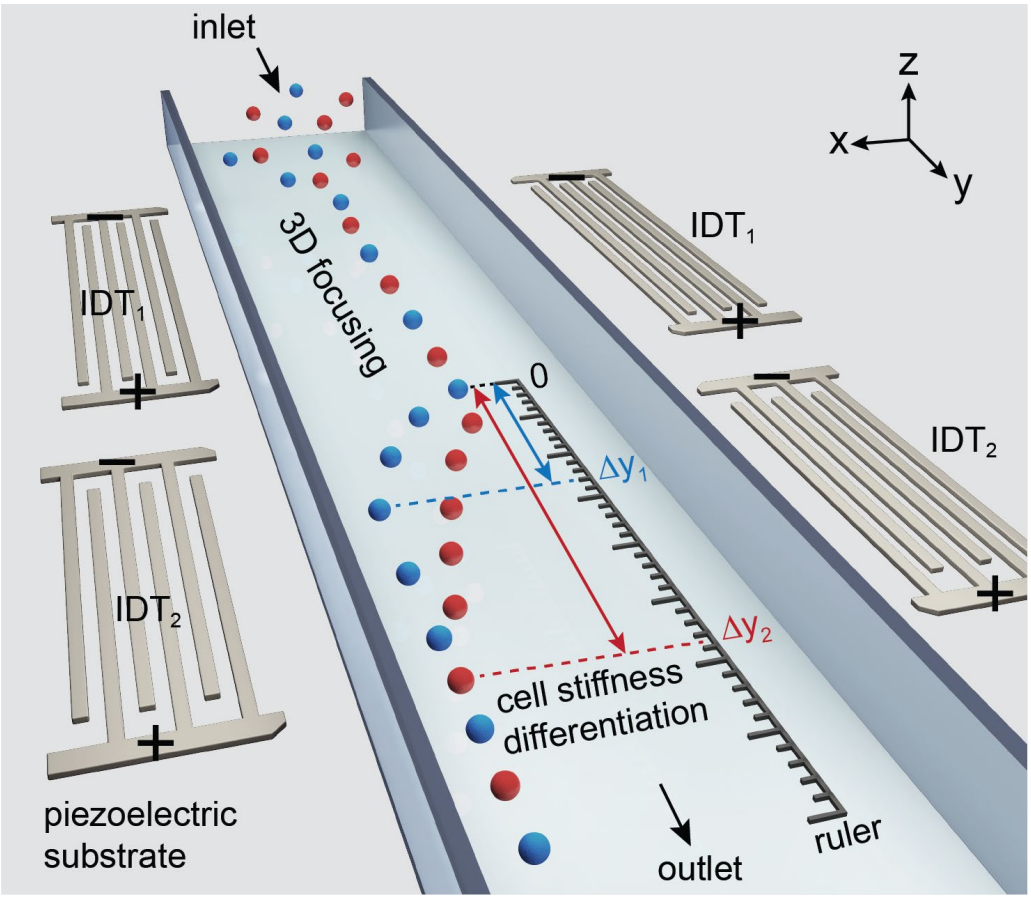

Figure 1.4.1: Principle of mechanical phenotyping via ON-SITE. Schematics of experimental setup showing an integrated ON-SITE platform that consists of two pairs of interdigital transducers (IDTs) and a flat-walled, short microfluidic channel. ON-SITE enables a two-level cascade of acousto-dynamic manipulation of living cells, yielding two 3D tightly focused and

diverted streams in a consecutive manner. The horizontal (channel length) project length Δy of the diverted cell stream is a function of cell compressibility. Movement of stiff (soft) cells that are represented by the blue (red) spheres yield a short (long) project length Δy.

Chapter 2

Device Design, Fabrication and Simulation

2.1 Photomask Design

The photomask is designed based on simulation and experimental requirement. Designing photomask by CAD software to determine channel construction and IDT geometry for getting excellent IDTs with a maximum quality factor (Q-factor) at a desired output standing acoustic wave wavelength, determining the particularly microfluidic geometry. The two sequential IDTs are the same except the shift between two IDTs in x axis direction. In order to generate standing acoustic wave, the wavelength of IDTs and the width of microchannel should be equal. In this project, the width of channel should be wide enough to make sure applying strong acoustic force to manipulate cells because the diameters of the cells we studied are generally large (6-8 μm). And based on relevant research we did before, we are very familiar with the 300 μm width system. Consequently, the microchannel is also set to 300 μm wide this time. Considering the sound velocity in the $LiNO_3$ substrate ($v \approx 3850$ m/s), the experimental frequency is determined by wavelength (λ = 300 μm, f = 12.8 MHz)[39]. The related parameters are determined experimentally, including definite number of finger pairs, contacting area of the pattern, and the distance between the two sequential IDTs. In our simulations, a set of 'focusing' and 'diverting' acoustic transducers with N_{IDT} = 25 finger pairs and

P_{IDT} periodicity were placed on a 500 µm thick 128° *Y*-cut *X*-propagating lithium niobate ($LiNbO_3$) piezoelectric crystal. The two pairs of IDTs were set to $16\lambda_{IDT}$ wide and positioned parallel to the channel sidewalls. The combination of these electrode features ensures strong electro-acoustic power conversion and minimal diffraction effect caused by amplitude distortions across the beam width[40], leading to efficient generation of surface acoustic waves (SAWs) via inverse piezoelectric effect. Meanwhile, to utilize probe to connect IDTs and RF generator, the length of contacting area is 6.8 mm. The spacing between the two IDTs is set to be contacted with probe conveniently. In a result, the IDT photomask are demonstrated in Figure 2.1.1:

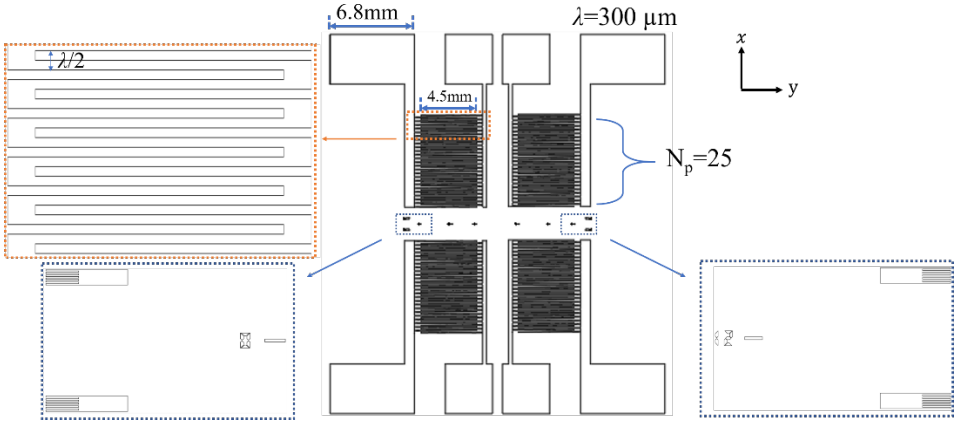

Figure 2.1.1: This figure demonstrates a CAD drawing of IDTs used for fabrication. The blue arrows point to fabricated alignment makers, assisting with alignment of the channel during bonding. Wavelength is 300 µm and the pattern consists of 25 pairs of fingers. The orange arrow points to fabricated fingers. The width of a finger and the spacing width between a finger and a finger are both $\lambda/4$. Therefore, the width of a pair of fingers is λ.

2.2 Fabrication

2.2.1 Microfluidic Fabrication

First and foremost, fabricating the PDMS microchannels with 110 μm high by using soft lithography techniques, which is described in Figure 2.2.1. Desired height can prevent almost 95% particles or cells from capturing on surface of microchannels. It shows the photolithography process and principle. Using Acetone and IPA to clean wafer and remove tiny greasy or oily residue via O_2 plasma at 80% power for 10 minutes. After that, a master consisting of a negative photoresist on the silicon wafer, is performed by pouring SU-8 2035 on the wafer and spinning it. Then soft bake strengths the curing, which is prior to 365 μm UV light exposure. Spinning rate, exposure and baking time depend on the target height of master. After UV exposure and hard baking, features will be developed by SU-8 developer. SU-8 developer helps to develop master and remove residues. The next step is to rinse the chip by DI water to make sure the master is smooth and clear. Therefore, pouring PDMS on the master and wait for heating curing treatment will generate a PDMS mold. the Sylgard 184 silicon elastomer kit is mixed at a 10:1 (30 grams: 3 grams) ratio of elastomer base to curing agent and then the mixture is degassed in a vacuum for approximately 45 minutes prior to casting. After heat curing for 3 hours in oven with 60 degrees, the PDMS molds are removed from the silicon master. A PDMS slab are produced by peeling the mold and cutting the slab to

individual devices. Finally, the ports are punched by biopsy punch. The width of ports depends on experimental requirement. Every single microchannel mold was cut from the casting and punch fluid reservoirs 1.5 mm wide by using a 1.5 mm biopsy punch.

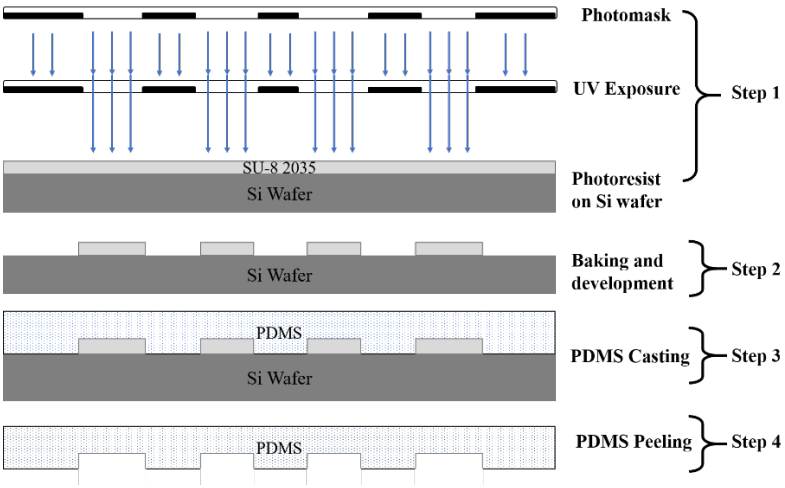

Figure 2.2.1: Soft lithography-based PDMS fabrication process, which consists of four main steps. A master consists of SU-8 photoresist, serving as a mold for PDMS, and the PDMS replica is sealed to a flat surface to enclose the channels.

2.2.2 IDT Fabrication

In our system, we use contact photolithography to determine and fabricate all IDTs on 128º YX $LiNbO_3$ piezoelectric substrate. To clean wafer by IPA and treat wafer in O_2 plasma at 80% power for 10 minutes prior to fabrication. In IDT fabrication process, the photoresist S1818 used to fabricate master has positive resistance, which is opposite to SU-8. The master is coated with a positive photoresist (S1818) by a spin coater with 2000 rpm. Soft bake on two hot plates

respectively, the wafer would be patterned with UV light at 190 units, the wafer's solubility is increased of the exposed areas. Note that it takes 25 seconds to develop target wafer by MF-319 developer to form the sacrificial layer for electrode patterning. If soak master too long or too short, the sacrificial layer would be over developed or undeveloped. After using MF-319 developer to remove the exposed areas, curing combination is performed by hard bake. After development, a 5 minutes oxygen plasma treatment of 70 w power in oxygen plasma will be performed to remove any residues in the developed regions. The next step, electron beam evaporation is utilized to deposit metal material on the surface of wafer, Ti (5 nm) and Au (120 nm). Deposition of these metal materials are carried out to get metal layers at 0.2 Å/s and 0.8 Å/s, respectively. After evaporation, the sacrificial layer of master placed into acetone is removed by sonication. Finally, the wafer is washed by rinsing whole wafer with DI water and it is diced into individual devices by a diamond scribe. The process flow is given below in Figure 2.2.2:

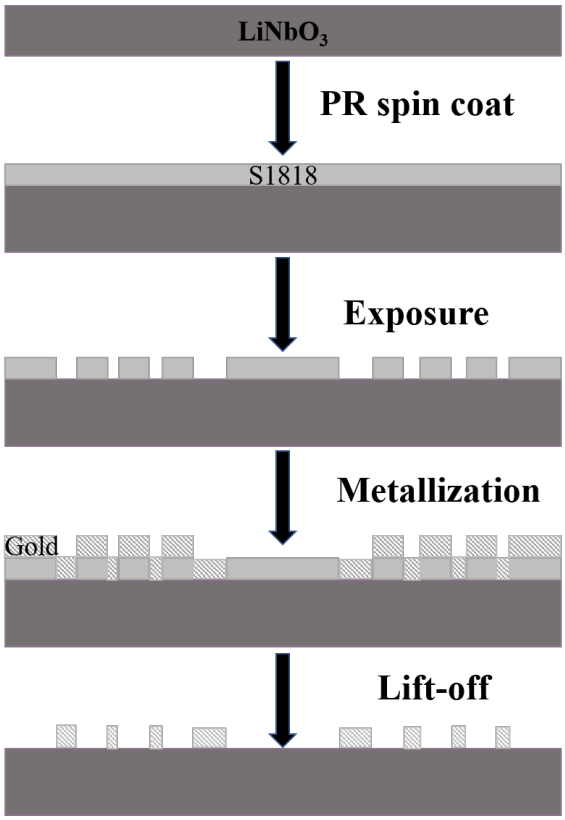

Figure 2.2.2: IDT fabrication process. After coating a photoresist, the wafers are deposited on a metal layer of Ti and Au. The sacrificial layer is removed via ultrasonication in acetone, and the process is called 'lift off'.

2.2.3 IDT Insertion Loss

Once a signal travels through a system in telecommunications, there is always loss of power resulting from the insertion of a device. The properties of a standing acoustic wave device rely on the measurement of the insertion loss detected between a pair of IDTs as a function of frequency. Therefore, after fabrications, it is very important to measure and report devices' insertion loss to make sure the

quality of devices is excellent. In order to test and determine the parameter and resonant frequency f_0 of the IDTs, a Planar TR 1300 single vector network analyzer (VNA) with two ports is utilized to measure the S parameters, S_{11} and S_{21} of the IDTs, which are input port voltage reflection coefficient and forward voltage gain, respectively. The frequency range of VNA is from 5 MHz to 20 MHz. The S parameters of sequential IDTs are given in Figure 2.2.3:

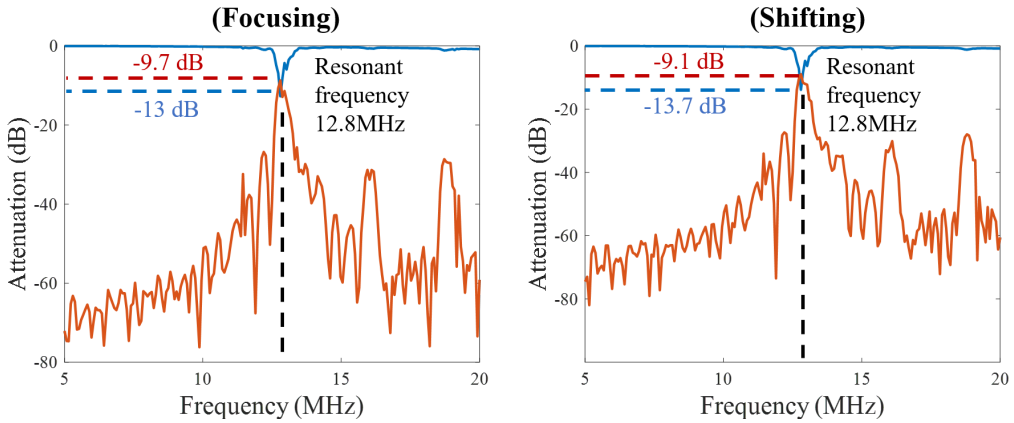

Figure 2.2.3: This figure shows the S parameters of sequential IDTs. The S parameters of the focusing and shifting IDTs performed by MATLAB. From this figure, we can see that the resonant frequency with max S_{21} and min S_{11} is 12.8 MHz. The parameters of focusing IDTs, S_{11} and S_{21} are -13 dB and -9.7 dB, respectively. And the parameters of shifting IDTs, S_{11} and S_{21} are -13.9 dB and -9.1 dB, respectively.

2.3 Experimental Setup

The experimental devices (Figure 2.3.1) are made by binding PDMS and IDTs. The surface of IDTs and individual PDMS mold are activated by UV-ozone and

then sealing PDMS to the accurate flat surface of IDTs to enclose the channels of PDMS. Set up is given in figure 2.3.1:

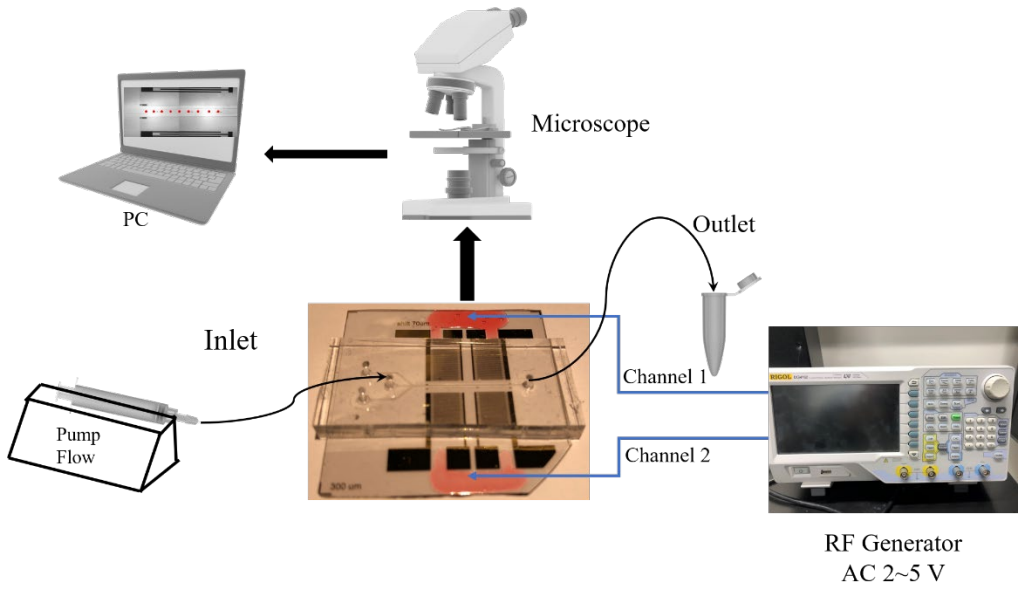

Figure 2.3.1: The setup mainly consists of microscope, three pumps, device, two RF generators and power. an alternating current (AC) signal to IDTs is generated by a RF generator. And the real time image will be transferred to computer so that we can observe the experimental process.

After binding PDMS and IDTs, to measure the device performance, utilizing 1mL syringes to pump phosphate buffered saline solution (PBS) into microchannel with 72 µL/hr via automatic syringe pumps. After pumping solution, the S parameters are measured again if there is no leaking. In the beginning of whole experimental process, the tested property of real images of microchannel transferred from microscope to PC makes sure that particles or cells can be seen on the screen of computer once pumping target solutions. Setting rate of main flow is 72 µL/hr. After seeing cells clearly, a RF generator with a two channels-AC signal

source with 50 Ω impedance is adjusted and simultaneously the applied signal to IDTs generates acoustic waves. Once the phenomena of immigration occur, the camera near the working microscope is turned on to record processes of focusing and shifting by Nikon software so that enabling us to analyze the immigration and properties of cells subsequently.

The microscope is conducted to get clear image on computer screen. After improvement, the image of IDTs and channel is shown in Figure 2.3.2:

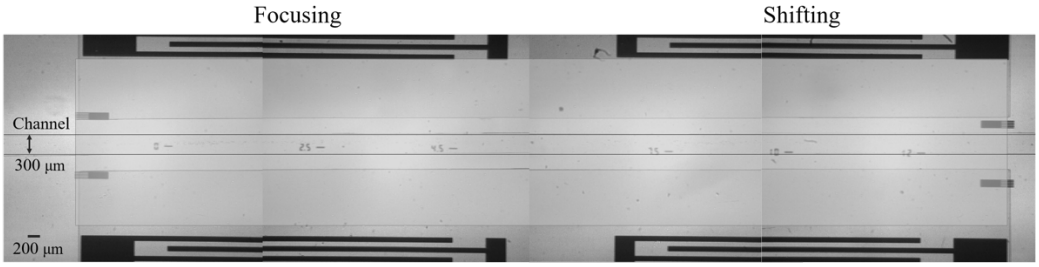

Figure 2.3.2: This figure shows the construction of the whole channel via microscope. Once the cells or particles are introduced into microchannel, their alignment can be seen in focusing region and their deflection in shifting region. The immigration of cells or particles depend on the sequential IDTs.

2.4 Stiffness Calculation and Simulation

2.4.1 ON-SITE Platform

To achieve the desired SSAW field distributions for cascaded 3D acousto-dynamic focusing and diverting, we carried out finite element method (FEM) simulations for SSAW and channel feature interactions (Figure 2.4.1). In our

simulations, a set of 'focusing' and 'diverting' acoustic transducers with N_{IDT} = 25 finger pairs and P_{IDT} periodicity were placed on a 500 μm thick 128° *Y*-cut *X*-propagating lithium niobate ($LiNbO_3$) piezoelectric crystal. The two pairs of IDTs were set to $16\lambda_{IDT}$ wide and positioned parallel to the channel sidewalls. The combination of these electrode features ensures strong electro-acoustic power conversion and minimal diffraction effect caused by amplitude distortions across the beam width[40], leading to efficient generation of surface acoustic waves (SAWs) via inverse piezoelectric effect. These one-dimensional surface-bound waves, in the form of atomic-scale surface displacements (~ 0.1 – 10 nm), propagate elastically on the surface of $LiNbO_3$ within a depth of approximately one acoustic wavelength λ_{IDT} that is equal to P_{IDT}. When encountering the fluid medium in the channel with P_{IDT} width, the SAWs decouple their orientation from the substrate by efficiently "leaking" into the fluid[41]. This energy radiation yields MPa-order compressional acoustic bulk wave (BAWs) propagating at a Rayleigh angle $\theta_R = \sin^{-1}(C_F/C_R)$ (C_F and C_R are the sound speeds of fluid and $LiNbO_3$, respectively)[42, 43]. To capture the coupling of BAWs with the channel boundaries, the PDMS walls are replaced using a lossy-wall boundary condition that is responsible for acoustic reflections at and acoustic refractions across all the PDMS/fluid interfaces[44].

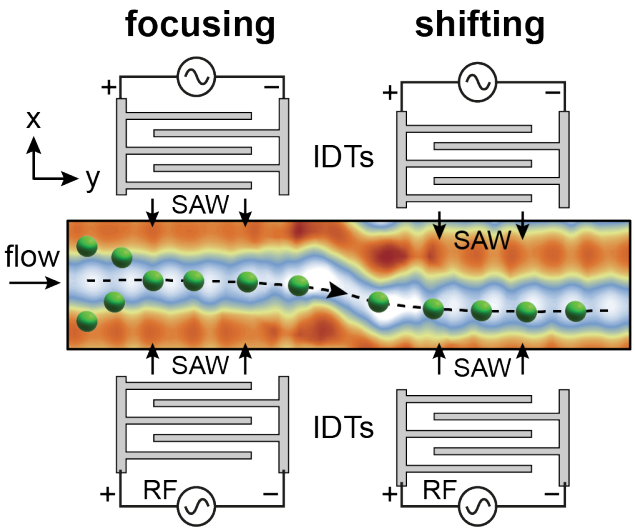

Figure 2.4.1: Schematic showing a top view of the ON-SITE platform. Numerical simulation of ARF potential in x–y plane is performed in both the 'focusing' and 'diverting' SSAW field regions. Movement of living cells marked by the green spheres is confined within the pressure minima locations (blue regions). A parabolic trajectory is formed after cells pass the 'diverting' SSAW field.

2.4.2 Acoustic Radiation Force

As shown in Figure 2.4.1, we observe a time-averaged absolute pressure $<P_1>$ field established in the *x-y* plane of the entire fluid domain. The pressure field consists of local minima (maxima) locations that are represented by the blue (red) regions. This periodic acoustic pressure field is essentially composed of two SSAW fields, which originate from the interference of the SAWs and their reflections from the PDMS walls. Interaction of cells suspended in the fluid with each SSAW field gives rise to a strong acoustic radiation force (ARF). According to the famous

acoustic formulation of the governing equations in perturbation theory, this time-averaged ARF acting on a cell of radius r_c ($r_c \ll \lambda_{IDT}$) in a standing wave can be expressed analytically step by step. The dynamic Navier-Stokes equation[45] for the velocity field is:

$$p = p(\rho), \tag{2.1}$$

$$\partial_t \rho = -\vec{\nabla}\cdot(\rho \vec{v}), \tag{2.2}$$

$$\rho \partial_t \vec{v} = -\vec{\nabla} p - \rho(\vec{v}\cdot\vec{\nabla})\vec{v} + \eta \vec{\nabla}^2 \vec{v} + \alpha\eta \vec{\nabla}(\vec{\nabla}\cdot\vec{v}). \tag{2.3}$$

where p and ρ are state expressing pressure and density, respectively. η is the dynamic viscosity of the fluid and α is the viscosity ratio typically of the order of unity.

Considering a quiescent liquid, we can post the constant density ρ_0 and pressure p_0. Once an acoustic wave presents and generates tiny perturbations to first and second order (subscript 1 and 2, respectively) in velocity v, pressure p, and density ρ. v is the vector of velocity[45-47]:

$$\vec{v} = \vec{v}_1 + \vec{v}_2, \tag{2.4}$$

$$p = p_0 + p_1 + p_2, \tag{2.5}$$

$$\rho = \rho_0 + \rho_1 + \rho_2. \tag{2.6}$$

Introducing the speed of sound c_0 of the fluid, which is:

$$c_0^2 = (\frac{\partial p}{\partial \rho})_s \tag{2.7}$$

Thus, pressure can be expressed by:

$$p_1 = c_0^2 \rho_1 \tag{2.8}$$

For most of the acoustophoretic applications, the $|\rho_1|/\rho_0 = |v_1|/c_0 < 10^{-3}$. Besides, the time-averaged acoustic velocity $|<v_2>|$ are smaller than $|v_1|$. Therefore, combining above equations, Navier-Stokes equation becomes:

$$\partial_t \rho_1 = -\rho_0 \vec{\nabla} \cdot \vec{v}_1, \tag{2.9}$$

$$\rho_0 \partial_t \vec{v}_1 = -c_0^2 \vec{\nabla} \rho_1 + \eta \vec{\nabla}^2 \vec{v}_1 + \alpha \eta \vec{\nabla} (\vec{\nabla} \cdot \vec{v}_1), \tag{2.10}$$

$$\partial_t^2 \rho_1 = c_0^2 [1 + \frac{(1+\alpha)\eta}{\rho_0 c_0^2} \partial_t] \vec{\nabla}^2 \rho_1. \tag{2.11}$$

An explicit expression for the compressibility β:

$$\beta = -\frac{1}{V}\frac{\partial V}{\partial p} = \frac{1}{\rho_0}\frac{\partial \rho}{\partial p} = \frac{1}{\rho_0 c_0^2}. \tag{2.13}$$

In response to an incoming wave v_{in}, we can describe v_1 by the incoming wave and an outgoing wave v_{sc}:

$$\vec{v}_1 = \vec{v}_{in} + \vec{v}_{sc}. \tag{2.12}$$

After discussing the field, we need to analysis the force of the filed on a compressible, spherical, micrometer-sized particle of radius r in a viscous fluid in an ultrasound field of wavelength λ, which requires that $r \ll \lambda$. Once the outgoing

wave has been determined for the incoming wave, the acoustic force on the particle can be calculate:

$$F_{ac} = -\int_{\partial\Omega} dr\{\langle p_2 \rangle \vec{n} + \rho_0 \left\langle (\vec{n}\cdot\vec{v}_1)\vec{v}_1 \right\rangle\}. \tag{2.13}$$

Consequently, acoustic force can be changed to be:

$$F_{ac} = -\int_{\partial\Omega} dr \left\{ [\frac{\beta}{2}\langle p_1^2 \rangle - \frac{\rho_0}{2}\langle v_1^2 \rangle]\vec{n} + \rho_0 \left\langle \left(\vec{n}\cdot\vec{v}_1\right)\vec{v}_1 \right\rangle \right\}. \tag{2.14}$$

To ease the determination of p_1 and v_1, using that in the inviscid bulk and they can be expressed by a velocity potential ϕ_1 which is expressed as $v_1=\nabla\phi_1$. Thus, Equation (2.3) implies:

$$\phi_1 = -i\frac{c_0^2}{\rho_0\omega}\rho_1, \tag{2.15}$$

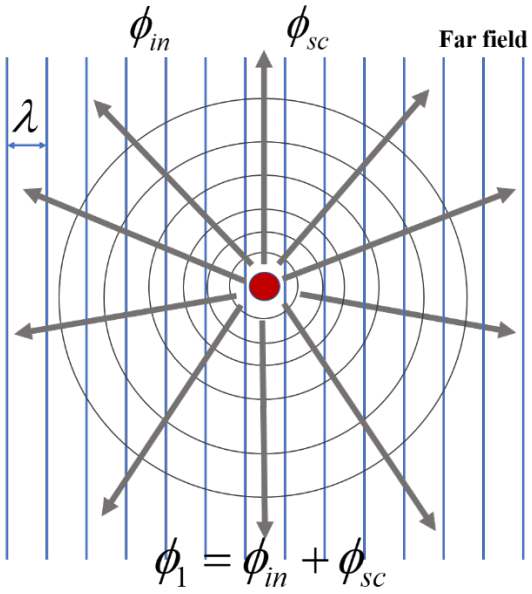

Figure 2.4.2: Sketch about velocity potential of far-field region. Illustrating the result incoming acoustic wave ϕ_{in} and outgoing scattered wave ϕ_{sc} with radius r ≪ λ. The first-order wave is $\phi_1 = \phi_{in} + \phi_{sc}$.

$$\phi_1 = \phi_{in} + \phi_{sc}, \tag{2.16}$$

$$\vec{v}_1 = \vec{\nabla}\phi_1 = \vec{\nabla}\phi_{in} + \vec{\nabla}\phi_{sc}, \tag{2.17}$$

$$p_1 = i\rho_0 w\phi_1. \tag{2.18}$$

$$F_{ac} = -\int_{\Omega} d\vec{r}\,\rho_0 \left\langle v_{in}(\vec{\nabla}^2 - \frac{1}{c_0^2}\partial_t^2)\phi_{sc} \right\rangle. \tag{2.19}$$

For standing wave considering ϕ_{in}, the acoustic force acting on a small particle ($r \ll \lambda$) is a gradient force:

$$F_{ac} = -\pi r^3 \{\frac{2\beta}{3}\mathrm{Re}[f_1^* p_{in}^* \vec{\nabla} p_{in}] - \rho_0 \mathrm{Re}[f_2^* \vec{v}_{in}^* \cdot \vec{\nabla}\vec{v}_{in}]\} \tag{2.20}$$

$$\vec{F}_{ac} = -\vec{\nabla} U^{ac}; \tag{2.21}$$

$$U^{ac} = \frac{4\pi}{3} r^3 \{\mathrm{Re}[f_1] \frac{\beta}{2} \left\langle p_{in}^2 \right\rangle - \mathrm{Re}[f_2] \frac{3\rho_0}{4} \left\langle v_{in}^2 \right\rangle\}. \tag{2.22}$$

Consequently, in our acoustic system, acoustic wave force can be determined by Equation (2.23):

$$F_{ac} = \frac{2\pi\alpha P_I \rho_s c_s r_c^3 \beta_f}{3 A_w \lambda_{\mathrm{IDT}}} \phi(\beta, \rho) \sin(2kx); \tag{2.23}$$

$$\phi(\beta, \rho) = \frac{5\rho_c - 2\rho_f}{2\rho_c + \rho_f} - \frac{\beta_c}{\beta_f}, \tag{2.24}$$

where $\phi(\beta, \rho)$ is the acoustophoretic contrast factor; ρ_f, ρ_c denote the density of the liquid and cell, respectively; β_f, β_c denote the compressibility of the fluid and cell, respectively; ρ_s, c_s denote the density and the sound speed of the substrate $LiNbO_3$, respectively. P_I denotes the power applied to the IDTs; α is the energy conversion efficiency from the applied electrical power to the acoustic pressure oscillations in the fluid; A_w is the working area which is a product of the channel length and the distance between the IDTs of each acoustic transducer; x determines the position of the cell within the field. In a typical cell-culture medium, the acoustic contrast factor $\phi(\beta, \rho)$, determining the ARF directionality, for cells is positive, which suggests that cell movement will be confined at the pressure minima locations (Figure 2.4.1). In microchannels, once a particle moves through liquid, it will experience a drag force that drives its movement. The flow follows stokes flow so

we can use Stokes' law to express drag force. Considering there are few particles or cells are elliptical even though most of cells are spherical, we need to discuss drag force with two situations.

2.4.3 Stokes Drag

When particles are introduced into microchannels, the incompressible flow can be described with the Stokes stream function ψ (ρ, z), which satisfies the differential equation[48]:

$$(\frac{\partial^2}{\partial\rho^2}-\frac{1}{\rho}\frac{\partial}{\partial\rho}+\frac{\partial^2}{\partial z^2})^2\psi=0. \tag{2.25}$$

If particles are elliptical, the prolate ellipsoid given in term of cylindrical polar coordinates (ρ, θ, z) by:

$$\frac{z^2}{s_0^2}+\frac{\rho^2}{s_0^2-1}=c^2. \tag{2.26}$$

In term of the inverse coordinates demonstrated by:

$$\begin{aligned} z' &= \frac{z}{\rho^2+z^2}; \\ \rho' &= \frac{\rho}{\rho^2+z^2}. \end{aligned} \tag{2.27}$$

Thus, the transformation Equation (2.27) shows that ψ / r^3 where $r^2 = \rho^2 + z^2$, satisfies that:

$$[\rho'\frac{\partial}{\partial\rho'}(\frac{1}{\rho'}\frac{\partial}{\partial\rho'})+\frac{\partial^2}{\partial z'^2}](\frac{\psi}{r^3})=0. \tag{2.28}$$

Particularly, adding χ to Equation (2.28), which is a function of ρ and z at regularly r = 0. And from Equation (2.27), $r^{-1} = r'$, if

$$\psi = \frac{1}{2}\rho^2(\frac{1}{r} - \chi), \tag{2.29}$$

then

$$\frac{\psi}{r^3} = \frac{1}{2}\rho'^2[1 - \frac{1}{r'}\chi]. \tag{2.30}$$

Accordingly, the drag force on the oblate body is $8\pi\mu v$ times coefficient of $-\rho'^2 / r'$ in the limit $r' \to \infty$. Where μ the dynamic viscosity of the fluid; v is the relative velocity between the fluid and the particle. Thus, the drag force is given by:

$$F_{drag} = -C_D \cdot 6\pi\mu v \cdot (\frac{S}{4\pi})^{\frac{1}{2}}. \tag{2.31}$$

Where C_D is the nondimensional drag coefficient, and S is the surface area of particles.

As for elliptical particles, S is given by:

$$S = \int_{-1}^{1} 2\pi \sqrt{(\frac{dz'^2}{dt})^2 + (\frac{d\rho'^2}{dt})} dt, \tag{2.32}$$

According to Equation (2.26), if $s = s_0$, then:

$$z = cst; \tag{2.33}$$

$$\rho = c(s^2 - 1)^{\frac{1}{2}} \cdot (1 - t^2)^{\frac{1}{2}}, \tag{2.34}$$

Consequently, combing Equation (2.32), Equation (2.33) and Equation (2.34) for elliptical particles, the S is:

$$S = \frac{2\pi}{c^2(s_0^2-1)}\left[\frac{s_0^2-1}{s_0^2} + \frac{s_0^2}{(2s_0^2-1)^{1/2}}\tan^{-1}\left\{\frac{(2s_0^2-1)^{1/2}}{s_0^2-1}\right\}\right]. \quad (2.35)$$

As for sphere, C_D is 1 and S is $4\pi R^2$. Specially, the drag force is given by:

$$F_{drag} = -6\pi\mu v R. \quad (2.36)$$

2.4.4 Time Dependent Particle Dynamics in Acousto-Fluidic systems

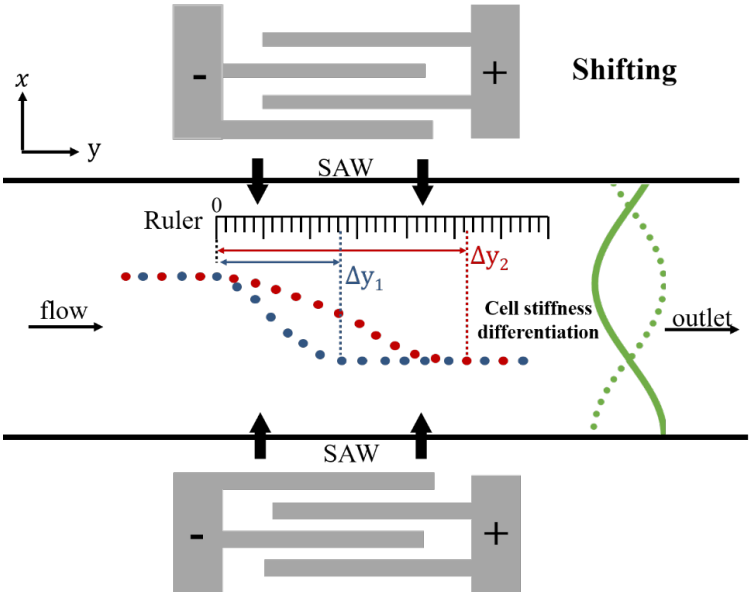

Figure 2.4.3: The competition between the two forces determines the migration and position of the cells in the deflection region.

Consequently, cells and particles will be subjected to acoustic force and drag force once they are introduced to IDTs regions. Cells' mechanical properties can be found with the help of the acoustic system comparing beads' trajectories and factors (time, size). Accordingly, the unknown compressibility of the cells can be found by the measurement of deflection and time from the tracked experimental

trajectories since the physical properties of standard polystyrene beads (density, size, and compressibility) are known.

In the channel, there is always a balance between acoustic wave force and fluid drag force[31, 32]:

$$F_{ac} = F_{drag}. \tag{2.37}$$

Combining Equation (2.23), (2.24), (2.36) and (2.37):

$$-6\pi\mu vR = -\frac{\pi P_0^2}{2\lambda}\cdot\frac{4}{3}\pi R^3\beta_m\left(\frac{5\rho_p - 2\rho_m}{2\rho_p + \rho_m} - \frac{\beta_p}{\beta_m}\right)\sin(2kx); \tag{2.38}$$

Therefore:

$$-6\pi\mu vR = \frac{2\pi\alpha P_1\rho_s c_s r_c^3\beta_f}{3A_w\lambda_{\mathrm{IDT}}}\phi(\beta,\rho)\sin(2kx). \tag{2.39}$$

We established an analytical model that can numerically capture the effects of multiple cell biophysical parameters (β_c, r_c, ρ_c) on its parabolic trajectory in the presence of the 'diverting' SSAW field (Supporting Information). In our model, we selected an input working frequency (12.8 MHz) and power (1.8 W/cm^2) for the 'diverting' IDT electrodes (P_{IDT} = 300 μm) and only took into account the ARF and hydrodynamic drag force. We first studied the effect of compressibility on cell trajectory by varying β_c of living cells within a typical compressibility range (3.5 – 4.2 ×10^{-10} Pa^{-1})[49]. Figure 2.4.4 shows the simulated trajectories of cells (r_c = 3 μm, ρ_c = 1084 kg/m^3) with different compressibilities (β_c = 3.8, 4.0, 4.2 ×10^{-10} Pa^{-1}) in

an aqueous medium (ρ_f = 1000 kg/m^3, β_f = 4.4 ×10^{-10} Pa^{-1}). We observe that the cells with a higher compressibility travel over a longer distance in the channel. According to our analytical model, we can establish a mathematical link between β_c and Δy by the following equation:

$$\Delta y = f(r_c, \beta_c, \rho_c) = \frac{C}{r_c^2 \phi(\beta_c, \rho_c)}. \tag{2.40}$$

where $C = 9\mu A_w \lambda_{IDT} x v_y / \alpha P_I \rho_s c_s \beta_f \sin(2kx)$, v_y is the cell velocity in axial direction and μ is the fluid viscosity.

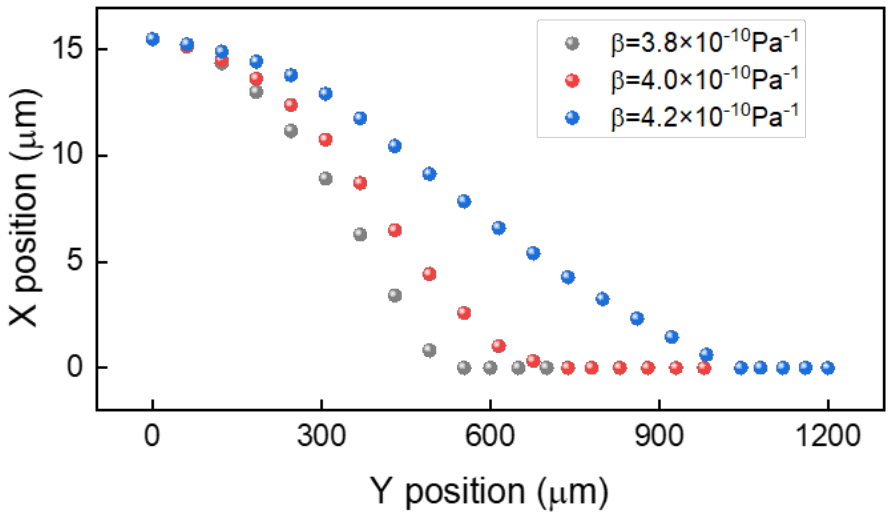

Figure 2.4.4: Simulated trajectories of cells with three different compressibility parameters (β_c = 3.8, 4.0, 4.2 ×10^{-10} Pa^{-1}) in the presence of both the 'focusing' and 'diverting' SSAW fields.

From Equation (2.40), we notice that analysis of cell trajectory merely, however, does not lead to accurate quantification of cell compressibility since cell size and density play important roles in cell migration behavior. To deconvolve these particular biophysical parameters from cell compressibility-dependent effect,

we performed parametric studies of the cell size and density effects (Figure 2.4.5 and Figure 2.4.6). In our parametric studies, the cell size and density parameters were varied over suitable ranges. We first studied the effect of cell size on cell compressibility measurement. Cell axial transit path lengths (Δy) over its entire parabolic trajectory for varying parameters (β_c, r_c) are presented in a two-dimensional (2D) heat map in Figure 2.4.5. Here, we observe that larger, stiffer (smaller, softer) cells yield shorter (longer) transit lengths (Δy), which are represented by the blue (red) regions. This 2D graph provides unambiguous guidelines for cross-examining the effects of cell size and compressibility on cell movement and allows one to readily classify cells into multiple categories by just measuring the cell axial transit path length.

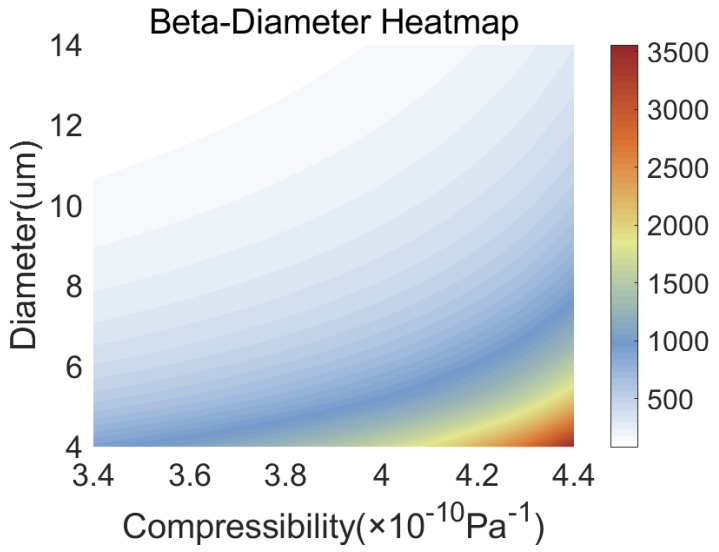

Figure 2.4.5: Parametric studies of cell size and compressibility (β_c, r_c) on cell transit path length Δy over its entire parabolic trajectory.

We then analyzed the relationship between the spread of cell density ρ_c and the measurement accuracy of cell compressibility. For bone-marrow derived HSCs capable of long-term hematopoietic reconstitution, their densities are normally 1084 ± 3 kg/m^3 with ± 0.3%[50] density spread. Using Equation (2.40), our analytical calculation shows that the corresponding measurement error represented by deviation in the quantification of cell compressibility falls into a narrow range ± 0.3% (Figure 2.4.6). This extremely small deviation value essentially sets the ultimate resolution limit of our ON-SITE measurement, which is superior to existing acoustic platforms for profiling of cellular mechanical properties[31-34].

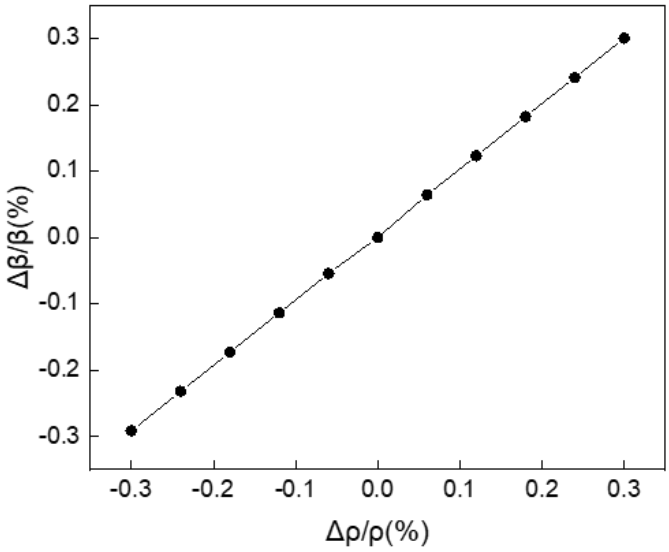

Figure 2.4.6: Study of cell density effect on cell compressibility measurement.

Chapter 3

Results and Discussion

3.1 Experimental validation of ON-SITE

To experimentally demonstrate the working principle of ON-SITE, we used polystyrene-based elastic modulus model particles with defined mechanical properties to investigate 3D focusing and diverting within the microchannel. A solution (2×10^5 particles/mL) of monodisperse polystyrene particles (Spherotech; r_p = 3.5 μm, ρ_p = 1050 kg/m^3, β_p = 2.16 ×10^{-10} Pa^{-1}) was prepared in phosphate buffered saline (PBS) and injected into the microchannel using a syringe pump (New Era Pump Systems). These cell-like microparticles were used as model particles with well-defined biophysical properties. A scientific-CMOS camera (Andor) was attached to the microscope to capture images and real-time videos of the movement and distribution of these microparticles during the 3D focusing and diverting processes. During the experiment, the IDT frequency, the input power, and the flow rate were set to 12.8 MHz, 1.8 W/cm^2, 72 μL/hr, respectively. In the region I, the microparticles were located outside the working area of the 'focusing' IDTs, hence the distribution of the particles in this region was uniform across the width of the channel (Figure 3.1.1). When the microparticles entered the 'focusing' SSAW field (region II), the ARFs acting on the particles aligned them at the center of the microchannel rapidly and tightly, where coincides with the pressure minima

locations (Figure 3.1.1). As the microparticles exited from the region II, they were focused into a narrow stream in three dimensions, flowing along the central axis of the channel at constant velocity (~ 1.3 mm/s). The width of the particle stream is comparable to the particle size and remained unchanged due to the laminar nature of the microfluidic flow[51]. Subsequently, when the microparticles entered the 'diverting' SSAW field, they were displaced towards the new pressure minima locations that are relatively shifted by 16 μm along the *x*-axis with respect to the initial pressure minima locations. Before the particles arrived at the new equilibrium locations, they traced out a parabolic trajectory.

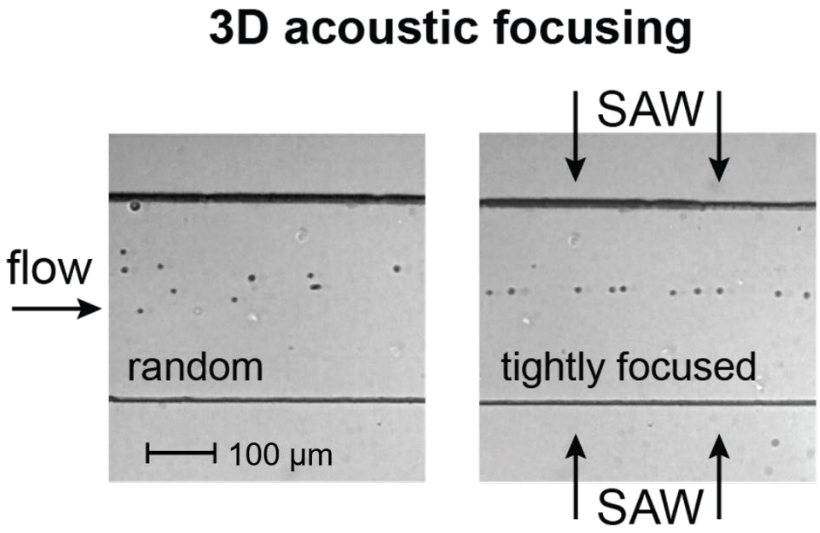

Figure 3.1.1: Characterization of the performance of ON-SITE-based 3D tight focusing of random suspensions of cell-like microparticles (r_p = 3.5 μm) when the 'focusing' SSAW field is absent and present. Scale bar: 100 μm.

We developed a custom-built image processing program enabling us to extract sets of spatial coordinate data from recorded particle trajectories. As shown in Figure 3.1.2, the measured particle trajectory (solid green curve) shows a parabola-like shape, which is in excellent agreement with our model prediction (dashed green curve). To further validate our analytical model, we repeated the above experiment with test polystyrene microparticles of a different size (r_p = 2 μm). We observe that the measured particle trajectory (solid red curve) again takes a similar shape of a parabola to that of the model particles (solid red curve), yet exhibits a relatively larger arc length. Such extended flight path is due to the fact that ARFs acting on smaller particles are weaker; thereby requiring a longer transit time for the particles to move to the pressure minima locations. We employed our analytical model to determine the compressibility parameter of the test particles by fitting the calculated trajectory (dashed red curve) with the measured one (Figure 3.1.2).

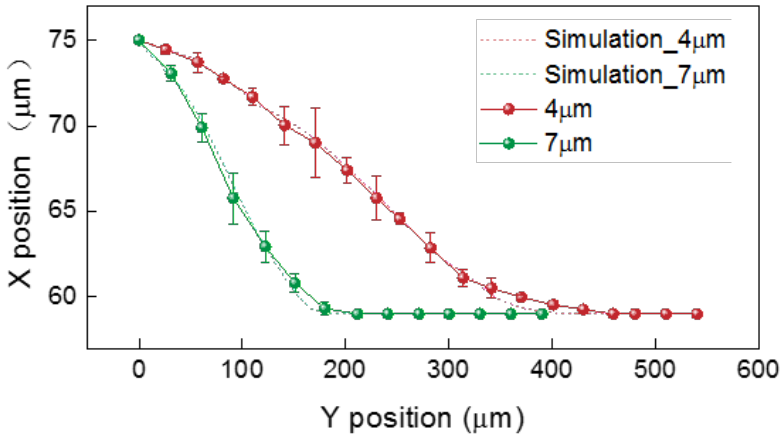

Figure 3.1.2: Measured trajectories of the model (r_p = 3.5 μm, green) and test (r_p = 2 μm, red) microparticles.

In this work, we study the mechanical properties of bone marrow derived hematopoietic stem cells (HSCs), myeloid progenitors (MyPro), and macrophages (Mac) due to their important significance for clinical purposes such as treatment of multiple myeloma and autoimmune disorders. We exploit ON-SITE to identify and distinguish HSCs from differentiated myeloid progenitors and macrophage cells.

3.2 High-throughput single cell mechanophenotyping

Understanding the intrinsic mechanical properties of HSCs and their differentiated progenies that govern cellular behavior and functions is instrumental not only for basic stem cell research, but also in the light of their clinical therapeutic relevance (e.g. treating hematological diseases)[52, 53]. Here, we investigated whether ON-SITE could distinguish between native and reprogrammed cell states in three different types of hematopoietic progenitors based on their mechanical properties. In our experiments, HSCs and their progenies - myeloid progenitors (MyPros) and macrophages (Macs) were selected. These three different lineage cells are typical representatives of hematopoietic hierarchy at different levels, spanning from multipotent to unipotent progenitors[53]. We used a standard ROCK inhibitor Y-27632 dihydrochloride to reprogram these mouse bone marrow-derived hematopoietic cell types by inhibiting the formation of intracellular filamentous actin (F-actin) stress fibers. The cells were incubated for 15 min with Y-27632, which results in decreased phosphorylation of cofilin and myosin light chain[54, 55].

Figure 3.2.1 presents two representative scanning electron microscopy (SEM) images of native and Y-27632 treated Mac. We observe a noticeable change in cell morphology and surface roughness during the treatment of cells with the ROCK inhibitor. This appreciable difference is possibly associated to enhanced active microtubule growth beyond its cytoplasm boundaries through Y27632 inhibition of the ROCK/Rho pathway[56].

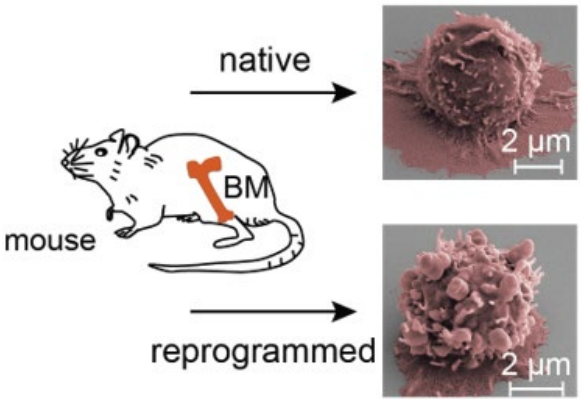

Figure 3.2.1: Three different murine hematopoietic cell types and their reprogrammed counterparts upon treatment with cytoskeleton-perturbing molecules were prepared. Scanning electron microscopy (SEM) images show the morphology and surface roughness of native and reprogrammed mature macrophage (Mac) cells.

To explore the difference in the mechanical properties between the native and reprogrammed cells, we performed ON-SITE experiments on native HSCs, MyPros, Macs and their Y-27632 treated counterparts under the same conditions as those on microparticles. We found a progressive increase in cell axial transit path length among both native (Figure 3.2.2) and reprogrammed (Figure 3.2.3) HSCs, MyPros,

Macs, suggesting a gradual increase in cell compressibility. Compared to the native counterparts, the reprogrammed cells showed minimal alterations in cell size, yet traveled over a longer distance. The observed larger cell transit length originates from an elevated level of the elastic modulus of the reprogrammed cells.

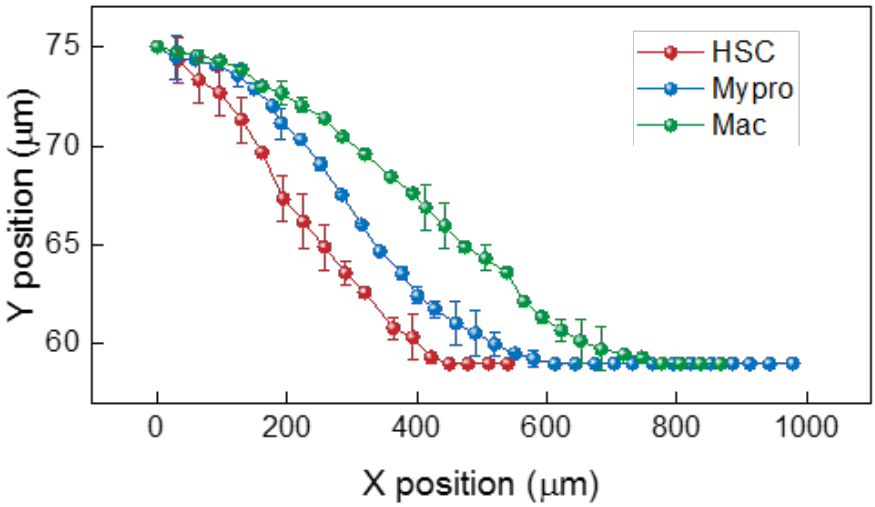

Figure 3.2.2: Measured trajectories of native cells. With the 16 μm shift, the cell axial transit path lengths of HSC, Mypro, and Mac are 450 μm, 612.14 μm, and 777.18 μm, respectively. It shows lowest hierarchical level of cells moves farthest among these diversities. Therefore, the order of cell compressibility for the three native target cells is HSC < Mypro < Mac.

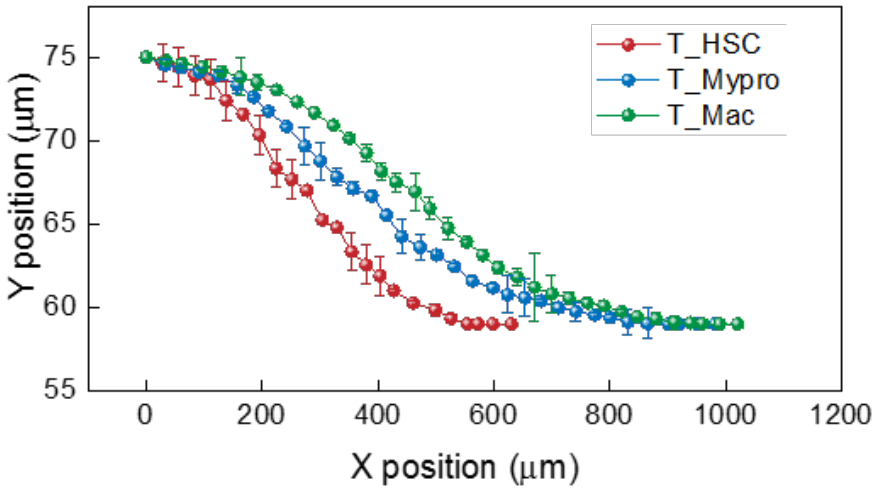

Figure 3.2.3: Measured trajectories of reprogrammed cells. With the 16 μm shift, the cell axial transit path lengths of treated HSC, treated Mypro, and treated Mac are 630.33 μm, 981.37 μm, and 1021.13 μm, respectively. It also announces that order of cell compressibility for the three treated cells is T_HSC < T_Mpro < T_Mac. And treated cells move farther than native cells.

3.3 ON-SITE Quantification of Cell Compressibility

To quantify cell compressibility of both native and reprogrammed hematopoietic cells, we applied our analytical model to deduce the parameter directly from its axial transit path length. In our test, we analyzed six large population of cells of different compressibility and size with a throughput of about 5×10^4 cells/hr. This remarkably high throughput is nearly 10,000-fold larger than gold standard mechanophenotyping technologies[12-15, 57, 58] and approximately 100-fold improvement compared to previously reported acoustic methods without microfluidic flow[31]. We used the aforementioned custom-built image processing program to determine the diameter of interrogated cells. Cell densities were set to

be 1.084 ± 0.003 kg/m^3 with a density spread of ± 0.3%[50]. The spread of cell density was set to be ±0.3%. As shown in Figure 3.3.1, the mean compressibility of the native HSCs, MyPros, Mac's was 3.69 ± 0.18 ×10^{-10} Pa^{-1}, 3.82 ± 0.27 ×10^{-10} Pa^{-1}, 4.02 ± 0.12 ×10^{-10} Pa^{-1}, respectively; and the mean compressibility of the reprogrammed ones was 3.89 ± 0.15 ×10^{-10} Pa^{-1}, 4.14 ± 0.07 ×10^{-10} Pa^{-1}, 4.16 ± 0.06 ×10^{-10} Pa^{-1}, respectively. These data show that the native cells are stiffer than the reprogrammed ones; and the native cells exhibit larger cell-cell variability in compressibility with respect to their reprogrammed counterparts. In addition, our results indicate that the inhibition of the ROCK/Rho pathway is immediate and only requires an extremely short incubation of Y-27632. The ability of our ON-SITE platform to identify subtle changes in cell phenotypes is two-fold. It not only enables us to distinguish native and reprogrammed cells at the population level, but also improves our understanding of the differences in cellular mechanical properties that arise as cells differentiate and their cytoskeleton is perturbed. As the hierarchical level increases, the compressibility becomes higher and the cells become softer. The normal distribution of the same cell decreases because of inhibitor. The order of cell compressibility is HSC < Mypro < Mac.

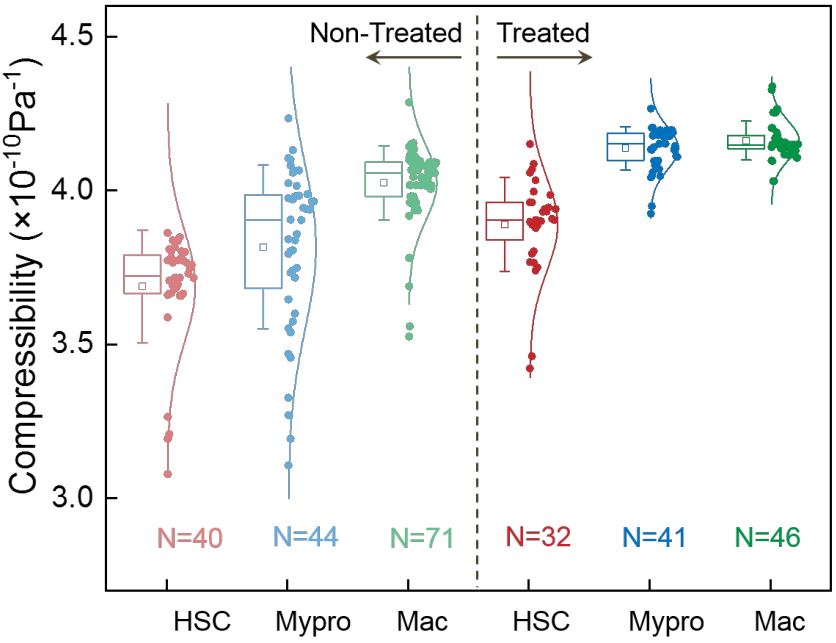

Figure 3.3.1: ON-SITE measures changes in the compressibility of hematopoietic cells treated with or without Y-27632 inhibitors. Six different large populations of cells including three native and three reprogrammed ones were interrogated. Quantification of cell compressibility via ON-SITE. Box plots denote the interquartile range (box hinges), means (squares), the error bars denote the standard deviation (whiskers), N is the number of cells measured from each population. The edges of the box correspond to 25% and 75% of the population.

The study of cell chemotaxis and migratory behavior is of particular interest in a wide range of biomedical research such as cancer metastasis or transplantation therapy[36, 59-61]. Regulation of ROCK/Rho signaling pathway plays an important role in controlling the actin cytoskeleton and chemotaxis in motile cells[62-64] but also endothelial barriers. To investigate the effect of Y-27632 treatment on cell migration ability, we utilized a Modified Boyden Transwell chamber assay to

assess the capacity of these hematopoietic cell types motility and invasiveness toward a chemo-attractant (agonist) gradient. Briefly, the Transwell chamber consists of two fluid chambers sandwiching a thin permeable 5 micron porous membrane, the pore diameter being slightly smaller than the size of cells of interest. Cells were suspended in culture medium were plated in the upper chamber; the lower chamber was filled with a solution containing a chemoattractant agent - recombinant murine SDF-1 (100 ng/ml). The directional migration of cells towards the chemoattractant through the porous membrane is reminiscent of a transendothelial migration process[65]. We quantified the number of migrated cells by flow cytometry analysis. As shown in Figure 3.3.2, there was a more than 2-fold increase in the cells migrating toward SDF-1 (shaded bars) in comparison to the migration buffer without SDF-1 (unshaded bars). In the presence of SDF-1, the order of the percentage of migrated native cells is HSCs (1.3 ± 0.32) < MyPros (6 ± 0.44) < Mac's (24.4 ± 2.62); the order for the migrated reprogrammed cells is HSCs (2.1 ± 0.67) < MyPros (8.3 ± 1.79) < Mac's (28.8 ± 2.46). Our result clearly shows that reprogrammed cells migrated better than the native ones, irrespective of the presence and absence of the chemoattractant. This is associated to the fact that it is easier for softer cells to conform their size to traverse through the relatively small pores, as compared to the stiffer cells.

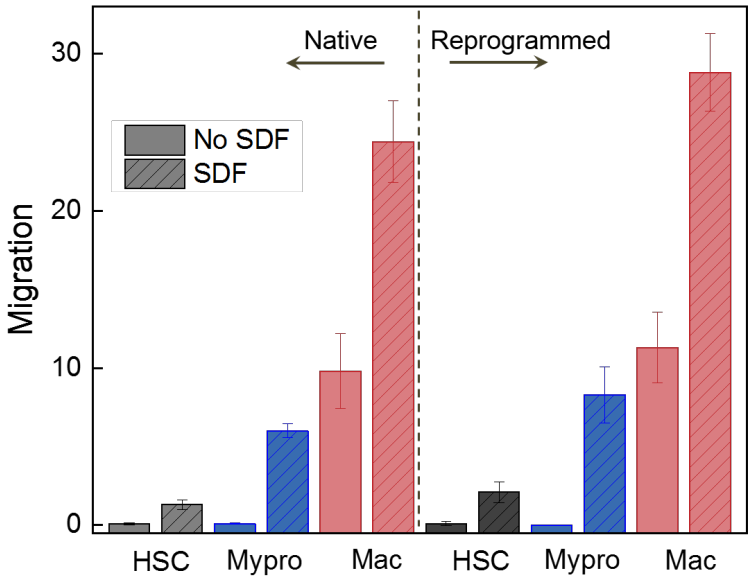

Figure 3.3.2: HSC, MyPro and Mac cells treated with or without Y-27632 inhibitors were allowed to migrate towards +/- SDF1 chemoattractant over 2 hrs.

Chapter 4

Conclusion

We have introduced a label-free, contactless, nON-invaSIve acousTo-mechanophEnotyping (ON-SITE) technology for accurate quantification of cellular mechanical properties. This unique ON-SITE scheme is based on a two-stage acousto-dynamic manipulation of living cells in continuous microfluid flow to yield cell mechanical properties-dependent trajectories. By merging three-dimensional cell focusing and touchless cell steering capabilities in a single platform, we realized in-situ, real-time, and high-throughput ($\sim 5 \times 10^4$ cells/hr) on-the-fly quantitative analysis of single-cell mechanics in a robust, accurate, and highly efficient manner. We developed an analytical model not only taking into account multiple biophysical factors including cell size, density, and compressibility, but also enabling us to effectively disentangle mutual contributions of these factors to the dynamic movement of cells. Using the model, we established a one-to-one mapping of cell elastic modulus to the cell transit path length over its trajectory. By tracking the full dynamics of suspended cells passing the ON-SITE actuation region, we demonstrated fast and quantitative probing of cellular mechanical properties using a regular inverted microscope setup equipped with a monochrome digital camera. We performed ON-SITE on hematopoietic cell types and determined elastic modulus properties for native hematopoietic stem cells, myeloid progenitors,

macrophages and their reprogrammed counterparts with altered intracellular cytoskeleton contractility within a single cell measurement. We studied cell migration ability by employing a Modified Boyden Transwell assay to evaluate the capacity of hematopoietic cell motility and invasiveness toward a chemo-attractant gradient. We observed significantly improved migratory ability during cell differentiation and when the ROCK/Rho signaling pathway is down-regulated. We believe our observation could provide unique insights into the intimate biophysical association between the compressibility of hematopoietic progenitors and their migration ability across a thin porous membrane that shares similar mechanical properties with the blood-tissue interface[66]. Therefore, ON-SITE holds great potential to be exploited as an efficient, label-free mechanophenotyping tool for basic biomedical research and clinical applications requiring an unbiased characterization of the mechanics of cells as well as cellular sub-populations at the single-cell level.

Bibliography

[1]. Dalaka, E., et al., *Direct measurement of vertical forces shows correlation between mechanical activity and proteolytic ability of invadopodia.* Science Advances, 2020. **6**(11): p. eaax6912.

[2]. Ladoux, B. and R.-M. Mège, *Mechanobiology of collective cell behaviours.* Nature Reviews Molecular Cell Biology, 2017. **18**(12): p. 743-757.

[3]. Marx, V., *May mechanobiology work forcefully for you.* Nature Methods, 2019. **16**(11): p. 1083-1086.

[4]. Fletcher, D.A. and R.D. Mullins, *Cell mechanics and the cytoskeleton.* Nature, 2010. **463**(7280): p. 485-492.

[5]. Holle, A.W., et al., *Cell-Extracellular Matrix Mechanobiology: Forceful Tools and Emerging Needs for Basic and Translational Research.* Nano letters, 2018. **18**(1): p. 1-8.

[6]. Lim, C.T., A. Bershadsky, and M.P. Sheetz, *Mechanobiology.* Journal of the Royal Society, Interface, 2010. **7 Suppl 3**(Suppl 3): p. S291-S293.

[7]. Urbanska, M., et al., *A comparison of microfluidic methods for high-throughput cell deformability measurements.* Nature methods, 2020.

[8]. Panciera, T., et al., *Mechanobiology of YAP and TAZ in physiology and disease.* Nature Reviews Molecular Cell Biology, 2017. **18**(12): p. 758-770.

[9]. Qiu, Y., D.R. Myers, and W.A. Lam, *The biophysics and mechanics of blood from a materials perspective.* Nature Reviews Materials, 2019. **4**(5): p. 294-311.

[10]. Chowdhury, F., et al., *Material properties of the cell dictate stress-induced spreading and differentiation in embryonic stem cells.* Nature materials, 2010. **9**(1): p. 82-88.

[11]. Wirtz, D., K. Konstantopoulos, and P.C. Searson, *The physics of cancer: the role of physical interactions and mechanical forces in metastasis.* Nature reviews. Cancer, 2011. **11**(7): p. 512-522.

[12]. Wu, P.-H., et al., *A comparison of methods to assess cell mechanical properties.* Nature methods, 2018. **15**(7): p. 491-498.

[13]. Dufrêne, Y.F., et al., *Imaging modes of atomic force microscopy for application in molecular and cell biology.* Nature nanotechnology, 2017. **12**(4): p. 295-307.

[14]. Pajerowski, J.D., et al., *Physical plasticity of the nucleus in stem cell differentiation.* Proceedings of the National Academy of Sciences, 2007. **104**(40): p. 15619-15624.

[15]. Hochmuth, R.M., *Micropipette aspiration of living cells.* Journal of Biomechanics, 2000. **33**(1): p. 15-22.

[16]. Lautenschläger, F., et al., *The regulatory role of cell mechanics for migration of differentiating myeloid cells.* Proceedings of the National Academy of Sciences, 2009. **106**(37): p. 15696-15701.

[17]. Ekpenyong, A.E., et al., *Viscoelastic properties of differentiating blood cells are fate- and function-dependent.* PloS one, 2012. **7**(9): p. e45237-e45237.

[18]. Kennedy, B.F., P. Wijesinghe, and D.D. Sampson, *The emergence of optical elastography in biomedicine.* Nature Photonics, 2017. **11**(4): p. 215-221.

[19]. Wang, N., J. Butler, and D. Ingber, *Mechanotransduction across the cell surface and through the cytoskeleton.* Science, 1993. **260**(5111): p. 1124-1127.

[20]. Gupta, S. and M. Guo, *Equilibrium and out-of-equilibrium mechanics of living mammalian cytoplasm.* Journal of the Mechanics and Physics of Solids, 2017. **107**.

[21]. Tseng, Y., T.P. Kole, and D. Wirtz, *Micromechanical mapping of live cells by multiple-particle-tracking microrheology.* Biophysical journal, 2002. **83**(6): p. 3162-3176.

[22]. Wu, P.-H., et al., *High-throughput ballistic injection nanorheology to measure cell mechanics.* Nature protocols, 2012. **7**(1): p. 155-170.

[23]. Otto, O., et al., *Real-time deformability cytometry: on-the-fly cell mechanical phenotyping.* Nature Methods, 2015. **12**(3): p. 199-202.

[24]. Huse, M., *Mechanical forces in the immune system.* Nature Reviews Immunology, 2017. **17**(11): p. 679-690.

[25]. Darling, E.M. and D.D. Carlo, *High-Throughput Assessment of Cellular Mechanical Properties.* Annual Review of Biomedical Engineering, 2015. **17**(1): p. 35-62.

[26]. Darling, E.M., S. Zauscher, and F. Guilak, *Viscoelastic properties of zonal articular chondrocytes measured by atomic force microscopy.* Osteoarthritis and Cartilage, 2006. **14**(6): p. 571-579.

[27]. Radmacher, M., et al., *Measuring the viscoelastic properties of human platelets with the atomic force microscope.* Biophysical journal, 1996. **70**(1): p. 556-567.

[28]. Davidson, P.M., et al., *High-throughput microfluidic micropipette aspiration device to probe time-scale dependent nuclear mechanics in intact cells.* bioRxiv, 2019: p. 641084.

[29]. Zhang, H. and K.-K. Liu, *Optical tweezers for single cells.* Journal of the Royal Society, Interface, 2008. **5**(24): p. 671-690.

[30]. Li, Y., Z. Guo, and S. Qu, *Living cell manipulation in a microfluidic device by femtosecond optical tweezers.* Optics and Lasers in Engineering, 2014. **55**: p. 150-154.

[31]. Hartono, D., et al., *On-chip measurements of cell compressibility via acoustic radiation.* Lab on a Chip, 2011. **11**(23): p. 4072-4080.

[32]. Wang, H., et al., *A continuous-flow acoustofluidic cytometer for single-cell mechanotyping.* Lab on a Chip, 2019. **19**(3): p. 387-393.

[33]. Kang, J.H., et al., *Noninvasive monitoring of single-cell mechanics by acoustic scattering.* Nature Methods, 2019. **16**(3): p. 263-269.

[34]. Augustsson, P., et al., *Iso-acoustic focusing of cells for size-insensitive acousto-mechanical phenotyping.* Nature Communications, 2016. **7**(1): p. 11556.

[35]. Beaudin, A.E., S.W. Boyer, and E.C. Forsberg, *Flk2/Flt3 promotes both myeloid and lymphoid development by expanding non-self-renewing multipotent hematopoietic progenitor cells.* Experimental hematology, 2014. **42**(3): p. 218-229.e4.

[36]. Smith-Berdan, S., et al., *Robo4 Cooperates with Cxcr4 to Specify Hematopoietic Stem Cell Localization to Bone Marrow Niches.* Cell Stem Cell, 2011. **8**(1): p. 72-83.

[37]. Boyer, S.W., et al., *All hematopoietic cells develop from hematopoietic stem cells through Flk2/Flt3-positive progenitor cells.* Cell stem cell, 2011. **9**(1): p. 64-73.

[38]. Smith-Berdan, S., et al., *ROBO4-mediated vascular integrity regulates the directionality of hematopoietic stem cell trafficking.* Stem cell reports, 2015. **4**(2): p. 255-268.

[39]. Chen, X., et al., *High performance lithium niobate surface acoustic wave transducers in the 4–12 GHz super high frequency range.* Journal of Vacuum Science & Technology B, 2015. **33**.

[40]. Devendran, C., et al., *Huygens-Fresnel Acoustic Interference and the Development of Robust Time-Averaged Patterns from Traveling Surface Acoustic Waves.* Physical Review Letters, 2017. **118**(15): p. 154501.

[41]. Gedge, M. and M. Hill, *Acoustofluidics 17: Theory and applications of surface acoustic wave devices for particle manipulation.* Lab on a Chip, 2012. **12**(17): p. 2998-3007.

[42]. Yeo, L.Y. and J.R. Friend, *Surface Acoustic Wave Microfluidics.* Annual Review of Fluid Mechanics, 2014. **46**(1): p. 379-406.

[43]. Collins, D.J., et al., *Two-dimensional single-cell patterning with one cell per well driven by surface acoustic waves.* Nature Communications, 2015. **6**: p. 8686.

[44]. Mao, Z., et al., *Experimental and numerical studies on standing surface acoustic wave microfluidics.* Lab on a Chip, 2016. **16**(3): p. 515-524.

[45]. Xie, Y., et al., *Probing Cell Deformability via Acoustically Actuated Bubbles.* Small, 2016. **12**(7): p. 902-10.

[46]. Bruus, H., *Acoustofluidics 2: perturbation theory and ultrasound resonance modes.* Lab Chip, 2012. **12**(1): p. 20-8.

[47]. Settnes, M. and H. Bruus, *Forces acting on a small particle in an acoustical field in a viscous fluid.* Physical Review E, 2012. **85**(1): p. 016327.

[48]. Davis, A.M.J. and K.B. Ranger, *A STOKES FLOW MODEL FOR THE DRAG ON A BLOOD CELL.* Quarterly of Applied Mathematics, 1987. **45**(2): p. 305-311.

[49]. Li, P., et al., *Acoustic separation of circulating tumor cells.* Proceedings of the National Academy of Sciences, 2015. **112**(16): p. 4970.

[50]. Juopperi, T.A., et al., *Isolation of bone marrow-derived stem cells using density-gradient separation.* Exp Hematol, 2007. **35**(2): p. 335-41.

[51]. Shi, J., et al., *Focusing microparticles in a microfluidic channel with standing surface acoustic waves (SSAW).* Lab on a Chip, 2008. **8**(2): p. 221-223.

[52]. Fonseca, A.-V. and D. Corbeil, *The hematopoietic stem cell polarization and migration: A dynamic link between RhoA signaling pathway, microtubule network and ganglioside-based membrane microdomains.* Communicative & integrative biology, 2011. **4**(2): p. 201-204.

[53]. Zhang, Y., et al., *Hematopoietic Hierarchy - An Updated Roadmap.* Trends Cell Biol, 2018. **28**(12): p. 976-986.

[54]. Maekawa, M., et al., *Signaling from Rho to the actin cytoskeleton through protein kinases ROCK and LIM-kinase.* Science, 1999. **285**(5429): p. 895-8.

[55]. Uehata, M., et al., *Calcium sensitization of smooth muscle mediated by a Rho-associated protein kinase in hypertension.* Nature, 1997. **389**(6654): p. 990-4.

[56]. Ory, E.C., et al., *Analysis of microtubule growth dynamics arising from altered actin network structure and contractility in breast tumor cells.* Physical biology, 2017. **14**(2): p. 026005-026005.

[57]. Bao, G. and S. Suresh, *Cell and molecular mechanics of biological materials.* Nature Materials, 2003. **2**(11): p. 715-725.

[58]. Van Vliet, K., G. Bao, and S. Suresh, *The biomechanics toolbox: Experimental approaches for living cells and biomolecules.* Acta Materialia, 2003. **51**: p. 5881-5905.

[59]. Justus, C.R., et al., *In vitro cell migration and invasion assays.* J Vis Exp, 2014(88).

[60]. Lauffenburger, D.A. and A.F. Horwitz, *Cell migration: a physically integrated molecular process.* Cell, 1996. **84**(3): p. 359-69.

[61]. Hall, A., *The cytoskeleton and cancer.* Cancer Metastasis Rev, 2009. **28**(1-2): p. 5-14.

[62]. Kümper, S. and C.J. Marshall, *ROCK-driven actomyosin contractility induces tissue stiffness and tumor growth.* Cancer cell, 2011. **19**(6): p. 695-697.

[63]. Ridley, A.J., *Rho GTPases and cell migration.* Journal of Cell Science, 2001. **114**(15): p. 2713-2722.

[64]. Fonseca, A.V., et al., *Polarization and migration of hematopoietic stem and progenitor cells rely on the RhoA/ROCK I pathway and an active reorganization of the microtubule network.* J Biol Chem, 2010. **285**(41): p. 31661-71.

[65]. Schaefer, A. and P.L. Hordijk, *Cell-stiffness-induced mechanosignaling – a key driver of leukocyte transendothelial migration.* Journal of Cell Science, 2015. **128**(13): p. 2221-2230.

[66]. Massberg, S., et al., *Immunosurveillance by hematopoietic progenitor cells trafficking through blood, lymph, and peripheral tissues.* Cell, 2007. **131**(5): p. 994-1008.